



RESEARCH ARTICLE

10.1002/2013JC009421

Key Points:

- Spice variance quantified along two sections
- QG/SQG theories not applicable
- Strong depth dependence

Correspondence to:

J. Klymak,
jklymak@uvic.ca

Citation:

Klymak, J. M., W. Crawford, M. H. Alford, J. A. MacKinnon, and R. Pinkel (2015), Along-isopycnal variability of spice in the North Pacific, *J. Geophys. Res. Oceans*, 120, 2287–2307, doi:10.1002/2013JC009421.

Received 11 SEP 2013

Accepted 22 FEB 2015

Accepted article online 25 FEB 2015

Published online 27 MAR 2015

Along-isopycnal variability of spice in the North Pacific

Jody M. Klymak¹, William Crawford², Matthew H. Alford³, Jennifer A. MacKinnon⁴, and Robert Pinkel⁴

¹Department of Physics and Astronomy, School of Earth and Ocean Sciences, University of Victoria, Victoria, British Columbia, Canada, ²Fisheries and Oceans Canada, Institute of Ocean Sciences, Sidney, British Columbia, Canada, ³Applied Physics Laboratory, University of Washington, Seattle, Washington, USA, ⁴Scripps Institution of Oceanography, University of California, San Diego, La Jolla, California, USA

Abstract Two hydrographic surveys in the Gulf of Alaska and the North Pacific subtropical gyre are presented. Both surveys are roughly perpendicular to lateral temperature gradients, and were collected in the summer when there was a shallow mixed layer and a seasonal thermocline. Isopycnal displacements and horizontal velocities are dominated by internal waves. Spice anomalies along isopycnals are examined to diagnose lateral stirring mechanisms. The spectra of spice anomaly gradients along near-surface isopycnals roughly follow power laws of $\sim k_x^{0.6 \pm 0.2}$ (variance spectra power laws of $\sim k_x^{-1.4 \pm 0.2}$), and in most cases, the spectra become redder at depth. The near-surface spectra are possibly consistent with the predictions of quasi-geostrophic turbulence theory (when surface buoyancy effects are accounted for), but the spectra at depth are inconsistent with any quasi-geostrophic theory. Probability distributions of spice gradients exhibit a large peak at low gradients and long tails for large gradients, symptomatic of fronts. Vertical coherence of the spice signal falls off with a decorrelation depth scale that has a maximum of about 80 m at 100 km wavelengths and depends on horizontal wavelength with a power law of approximately $k_x^{-1/2}$. Lateral decorrelation length scales are 20–40 km, close to the baroclinic Rossby radius. Lateral stirring occurs over large scales, with average lateral displacements of about 200 km in the upper 75 m, decreasing to 100 km at greater depths. The depth variation of the statistics indicates that time history of tracer stirring on each isopycnal is important, or that there are unconsidered depth-dependent stirring mechanisms.

1. Introduction

The ocean is stirred and mixed laterally along isopycnals as well as mixing vertically across isopycnals. Temperature and salinity properties in the upper ocean are largely set where each isopycnal outcrops at the surface, with a pattern set by disparate surface forcing [e.g., Todd *et al.*, 2012]. Once subducted, temperature and salinity are stirred along isopycnals by a variety of physical mechanisms, many of which are still active areas of research. Understanding the processes that stir the ocean laterally will help improve our understanding of seawater distributions and the global transport of heat.

Competing theories for dominant stirring physics may be differentiated, in part, by the statistical properties they produce in the stirred fluid. There is a small but growing literature documenting measurements of lateral variability on scales fine enough to capture a reasonable dynamic range of horizontal scales. Measurements spanning a wide range of scales are required to capture both the large-scale background gradient and the smaller-scale structures that the stirring produces. However, because temperature and salinity also vary with depth, direct horizontal tows are too contaminated by isopycnal heaving due to internal waves to yield useful results. Therefore, lateral observations need to be coupled with vertical information about density in order to track properties along isopycnal surfaces. The best method to capture the requisite physics, so far, appears to be using an undulating profiler towed behind a ship, or autonomous gliders. There are few such observations to date, notably work by Ferrari and Rudnick [2000], Callies and Ferrari [2013], Cole *et al.* [2010], and Cole and Rudnick [2012] who had SeaSoar or glider occupations along sections in the North Pacific. Glider observations in the California Current document the gradients between warm, salty nearshore water and cooler fresher water offshore [Todd *et al.*, 2012]. Here we add to these observations with one section in the North Pacific subpolar gyre, and a second in the subtropical gyre, both collected with undulating profilers. In addition to presenting spectra, we extend the analysis of such records in a few of simple ways by reporting the vertical scale at which the signals become incoherent with depth, the probability

This is an open access article under the terms of the Creative Commons Attribution-NonCommercial-NoDerivs License, which permits use and distribution in any medium, provided the original work is properly cited, the use is non-commercial and no modifications or adaptations are made.

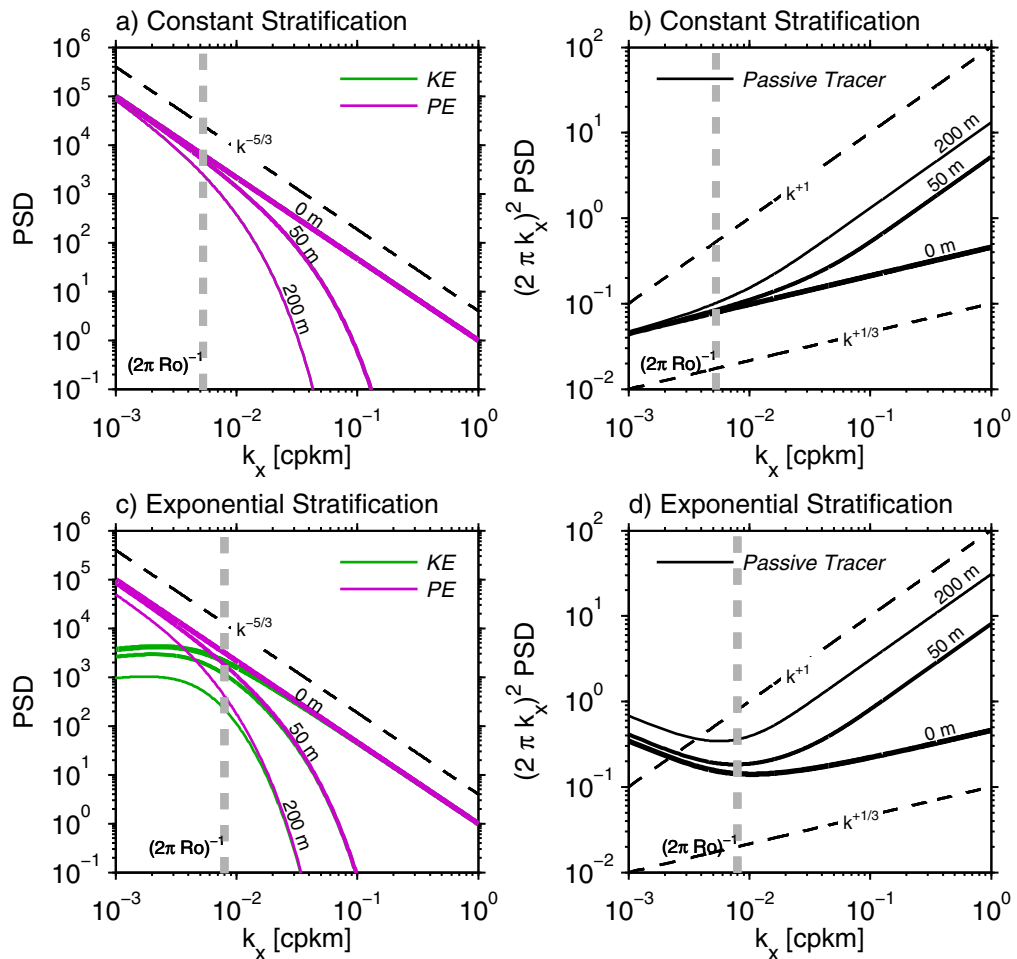


Figure 1. Theoretical spectral shapes for surface quasi-geostrophic turbulence. (a) Energy and (b) whitened passive tracer spectra for a constant-stratification with $N=8\times10^{-3}\text{s}^{-1}$ and $f=1.15\times10^{-4}\text{s}^{-1}$. (c) Energy and (d) passive tracer-gradient spectra for an exponential stratification, $N=8\times10^{-3}\text{s}^{-1}$, $f=0.77\times10^{-4}\text{s}^{-1}$, and stratification decay scale of 600 m. Spectra are shown for 0, 50, and 200 m depths. For all spectra, the surface potential energy spectrum is assumed to follow a $k_x^{-5/3}$ distribution. For constant stratification, the potential and kinetic energy spectra are identical. Energy spectra follow Callies and Ferrari [2013], and the tracer spectra are computed from the kinetic energy spectra following (Scott [2006] by numerical integration of his equations (10) and (13)).

distribution of the tracer gradients, the decorrelation lengths scales of spice along isopycnals, and the distance spice anomalies would have to be displaced from their ordered background distributions.

It is often useful to consider spectral estimates when characterizing variance of a turbulent field, and we do so below. The literature uses different conventions for presenting these spectra, so we clarify our convention here. We present spectra with wave numbers in units of cycles-per-kilometer (cpkm). We also present tracer-gradient spectra, in this case of spice anomaly gradients along isopycnals. We calculate tracer-gradient spectra by whitening the variance spectra: $\phi_{d\gamma/dx}=(2\pi k_x)^2 \phi_\gamma$, where k_x is in units of cpkm. Tracer-variance spectra are usually “red” (steep), so gradient spectra are flatter, allowing more dynamic range when plotting and power laws to be more easily differentiated by eye.

Theories predicting the spectra of turbulent properties assume that the spectra are in statistical equilibrium, with variance production in balance with its dissipation. There are a number of such theories, based on geostrophic turbulence concepts that can be readily expressed in terms of spectral power laws that depend on the direction of the energy and vorticity cascades (see Smith *et al.* [2002] and Vallis [2006], for a recent review). These theories are steady state, in that the input of vorticity is assumed constant, and the stirring of the tracers is posited to be in equilibrium with the input of large-scale tracer gradients. For quasi-geostrophic turbulence [Charney, 1971], tracers are stirred by eddies formed by low-vertical-mode baroclinic

instability, and tracer-gradient spectra are expected to follow K_h^{+1} for high wave numbers [Batchelor, 1959], where $K_h^2 = k_x^2 + k_y^2$ is the horizontal wave number. Because these motions have large vertical and horizontal scales, statistics are not expected to change significantly with depth.

Surface quasigeostrophy (SQG) further assumes that the source of vorticity is at the ocean surface with the potential energy spectra following a $\mathcal{P}(z=0, K_h) \sim K_h^{-5/3}$ power law. Under constant stratification, $N = \left(\frac{-g d\rho(z)}{\rho_0 dz} \right)^{1/2}$, and assuming no interior sources of potential vorticity, there is a decay in kinetic energy \mathcal{K} (K_h, z) $\sim \mathcal{P}(z=0, K_h) e^{\frac{K_h z N}{f}}$ (for $z < 0$), with high wave numbers (K_h) decaying faster than low (Figure 1a) [Scott, 2006]. In this regime, surface tracer-gradient spectra follow an inertial subrange spectra $K_h^{1/3}$, but deep spectra asymptote to K_h^{+1} , so we expect bluer (more high- K_h variance) spectra with depth (Figure 1b) [Scott, 2006]. As pointed out by LaCasce [2012] and Callies and Ferrari [2013], in an ocean with nonconstant stratification, potential energy will have a similar spectrum, but kinetic energy will have a pronounced roll-off at lower wave numbers (Figure 1c) [after Callies and Ferrari, 2013]. The effect of this roll-off is going to be difficult to discern in data because, for the parameters used here, the roll-off is most pronounced at scales larger than the first internal Rossby radius, where the dynamics are likely dominated by geostrophically balanced mesoscale structures. The effect of the roll-off on passive scalars is to drive more variance to higher wave numbers, and thus deep tracer spectra might be expected to be more blue (more high- k_x variance) than shallower spectra (Figure 1d). So, regardless of whether SQG is important near the surface, the spectral shape of tracer-gradient spectra at high wave numbers asymptote to K_h^{+1} .

Observationally, lateral spectra of spice along isopycnals have been considered by Cole *et al.* [2010] and Cole and Rudnick [2012], who report a k_x^0 passive scalar gradient slope out to 1/16 cpkm (note the full K_h spectrum is unavailable to observational methods). Similar results are reported by Ferrari and Rudnick [2000] and Callies and Ferrari [2013], including a tow that followed an isopycnal, giving high-wave number information. These papers point out that such a slope is inconsistent with SQG theories, and possibly imply stirring creating discontinuous fronts [Hoskins and Bretherton, 1972; Boyd, 1992]. Nonlinear frontogenesis was also invoked to explain steeper tracer-gradient slopes in high-resolution fully nonlinear numerical simulations [Capet *et al.*, 2008; Klein *et al.*, 2008]. The idea is that ageostrophic flows that are beyond SQG theory drive frontogenesis, and that this stirs the tracer beyond what SQG would predict, leading to redder tracer spectra. Below we also find a tracer-gradient slope much closer to k_x^0 than k_x^{+1} in our data. We test the idea that there is frontogenesis acting to sharpen small-scale gradients by checking the probability distribution functions of the spice gradient, which we show are quite peaked compared to a normal distribution, indicative of fronts.

The paradigm of QG/SQG stirring seems in doubt in ocean observations, but the frontogenesis alternative appears to have some difficulties as well. For instance, Cole and Rudnick [2012] found redder tracer spectra ($\sim k_x^0$) down to 1000 m, a depth beyond which surface-intensified fronts are expected to have a strong influence. We corroborate this finding with our significantly shallower data set by noting that some of our spectra get redder with depth rather than bluer. We also note that the coherence of the spice field falls off quickly with depth, implying that vertically coherent, surface-intensified motions are not likely the direct source of stirring at depth.

Below we outline our measurements (section 2), and then overview the observations (section 3). Internal waves are briefly discussed (section 4), partly to document the variability of the isopycnal heave and partly to validate the transfer function used to correct variance lost at high wave numbers due to profiler sampling (Appendix A). Next, we consider statistics of the spice field along isopycnals (section 5) using the statistics discussed above. The results are discussed in section 6.

2. Cruises and Instrumentation

Two cruises are discussed in this paper. The first was part of the regular Line P hydrographic work [Crawford *et al.*, 2007] during August of 2008. As the CCGS *Tully* steamed west from Vancouver Island to Station Papa conducting hydrography stations (Figure 2), we deployed a Moving Vessel Profiler (MVP 200, made by Rolls Royce Marine) between stations. The MVP is weighted, and drops freely at about 3 m/s as the ship steams, then is pulled back in by a winch. The ship averaged 5 m/s between stations, and profiles were made every

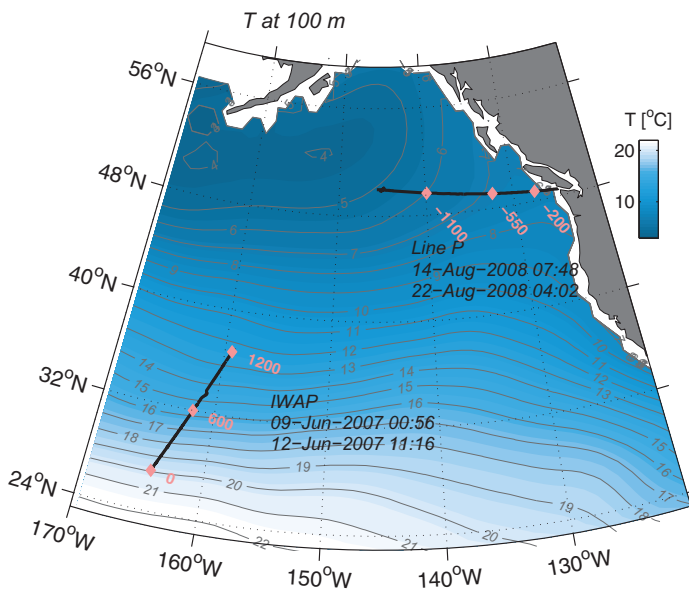


Figure 2. Maps showing IWAP and Line P lines, plotted over temperature from summer climatology at 100 m (World Ocean Atlas). Both lines have the x coordinate system used plotted at three points in pink: x in km is approximately north/south for the IWAP data and approximately east/west for the Line P data.

Soar towed from the *R/V Revelle* at 4 m/s, and equipped with a pair of Seabird 9/11 CTDs. Most undulating tow yos were made to 400 m depth, for a lateral spacing midcast of approximately 2.5 km. Details of the effect of the tow geometry on the spectra are discussed in the Appendix A. Concurrently, a 50 kHz Doppler sonar was collecting profiles of ocean currents to over 800 m depth in 16 m vertical bins (the Hydrographic Doppler Sonar System) [Pinkel *et al.*, 2003]. Five minute averages were formed and found to be largely noise free, giving a lateral spacing of approximately 1200 m. Detailed comparisons of this data set have been made with measurements from moorings deployed along the same line [MacKinnon *et al.*, 2013a, 2013b; A. J. Pickering *et al.*, manuscript in preparation, 2015]. Here we focus on the lateral variations in salt, temperature, and velocity.

Different response times of conductivity and temperature probes from both vehicles were matched by determining the phase lag between the probes to frequencies less than 3 Hz, beyond which the signals become incoherent. This reduces salinity spikes; thermal mass effects were not accounted for, as they are relatively small compared to temperature and salinity signals in the upper ocean [see Gregg and Hess, 1985; Ferrari and Rudnick, 2000, for more details].

3. Overviews

3.1. Line P

Line P runs from the Strait of Juan de Fuca to Station P at 50°N 145°W in the Alaskan Gyre [Crawford *et al.*, 2007]. The region is subject to strong winter mixing, producing mixed layers in excess of 100 m (Figure 3a). This surface water warms and restratifies in the summer (Figure 3b), creating a near-surface thermocline, a “remnant layer” to about 120 m, and a permanent thermocline beneath. A similar classification of upper ocean water due to spicce variance was used by Cole *et al.* [2010]. The remnant layer is largely stratified by salinity, whereas temperature acts as an almost passive tracer. Waters in midgyre are cooler and saltier than nearshore waters at the same depth, due to freshwater input at shore and wind-driven upwelling midgyre.

The MVP was used to collect data at 1.7 km lateral resolution along Line P (Figure 4a). The added resolution compared to the hydrographic sections gives a much clearer picture of the upper-ocean structure. Isopycnal excursions exceeding 20 m are evident, likely due to internal waves. Coherent T/S structures can be seen in the raw data, but are easier to track by transforming to isopycnal coordinates. We plot versus mean

340 s to 200 m depth, for a horizontal spacing of 1.7 km. Using a Seabird 49 CTD, the MVP measured temperature and salinity with approximately 1 m vertical resolution. Only downcasts were used for the analysis; upcasts tended to be relatively close to the location of downcasts for the deepest waters, and then followed a more horizontal path for the upper 40 m due to the lateral resistance of the water. The largely redundant extra information in the upcasts was not deemed useful.

The second cruise was part of the Internal Waves Across the Pacific experiment (IWAP) [Alford *et al.*, 2007] and run from 26°N to 39°N, north of the Hawaiian Ridge (Figure 2), in June 2007. The data consisted of tows with an undulating Sea-

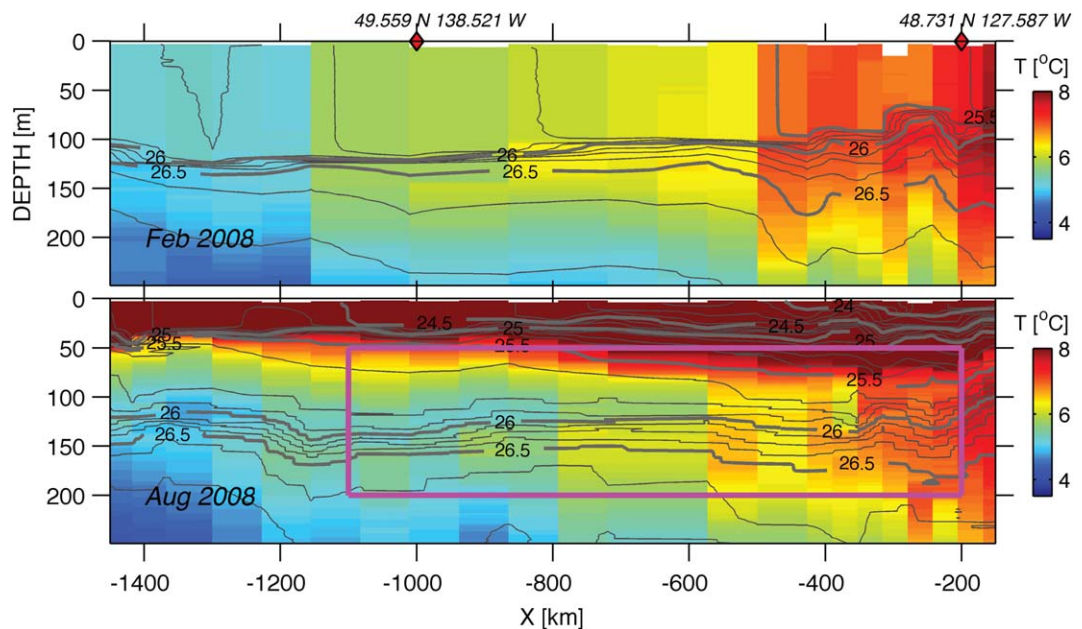


Figure 3. Line P CTD sections February 2008 and August 2008. Colors are temperature from individual CTD casts, contours are potential density. The magenta box is the region of the MVP sections.

isopycnal depths (Figure 4b; from here on out, “isopycnal depth” will be the coordinate used to describe isopycnals). Sharp gradients are present in both the vertical and horizontal.

The temperature shows vertically coherent structures in the seasonal thermocline (50–120 m), with the structure becoming more diffuse in the permanent thermocline (Figure 5). There is filamentation along the edges of the T/S fronts, indicative of the features being laterally stirred with the surrounding fluids. A bit of care needs to be taken when considering these plots in isopycnal space because there has been some interpolation in the vertical, which can tend to elongate filaments in the vertical. This should smooth gradients, rather than enhance them.

Spice is proportional to the temperature or salinity anomaly along an isopycnal, and is a convenient way to consider tracer stirring along isopycnals [Veronis, 1972]. We calculate this as the distance in T/S space from the mean T/S profile along an isopycnal, where the distance of the parcel is approximated linearly:

$$\gamma = \text{sgn}(T - \bar{T}) \left(\alpha^2 (T - \bar{T})^2 + \beta^2 (S - \bar{S})^2 \right)^{\frac{1}{2}}. \quad (1)$$

Here \bar{T} and \bar{S} are the mean temperature and salinity on the isopycnal, $\alpha = -\frac{d\rho}{dT}$, and $\beta = \frac{d\rho}{dS}$. This definition of spice depends on the mean profile across the section, and therefore is not globally invariant. The sign of spice is such that water that is warmer than average along the isopycnal has positive spice; units are density. For a given section, the mean spice along an isopycnal is approximately zero, with slight variations due to curvature of the equation of state. The linear approximation is good (Figure 6).

The resulting section of spice is similar to the images of temperature (Figure 4c) deeper than 60 m. Warm salty water (positive spice anomaly) is on the shoreward side of the section (low x) and cold-freshwater (negative spice anomaly) offshore. The spice gradient is opposite in shallower water where temperature dominates the density structure, and thus negative spice anomaly is onshore, and positive offshore.

3.2. IWAP

The IWAP cruise transited north to south for over 1200 km. It crossed the subtropical front approximately 300 km from the south end of the line (Figure 7). Temperature increases toward the south along a constant depth. As for Line P, heave due to isopycnals can be removed by considering spice along isopycnals, again plotted as “isopycnal depth,” and we compute spice from the mean T/S profile at each potential density (Figure 8).

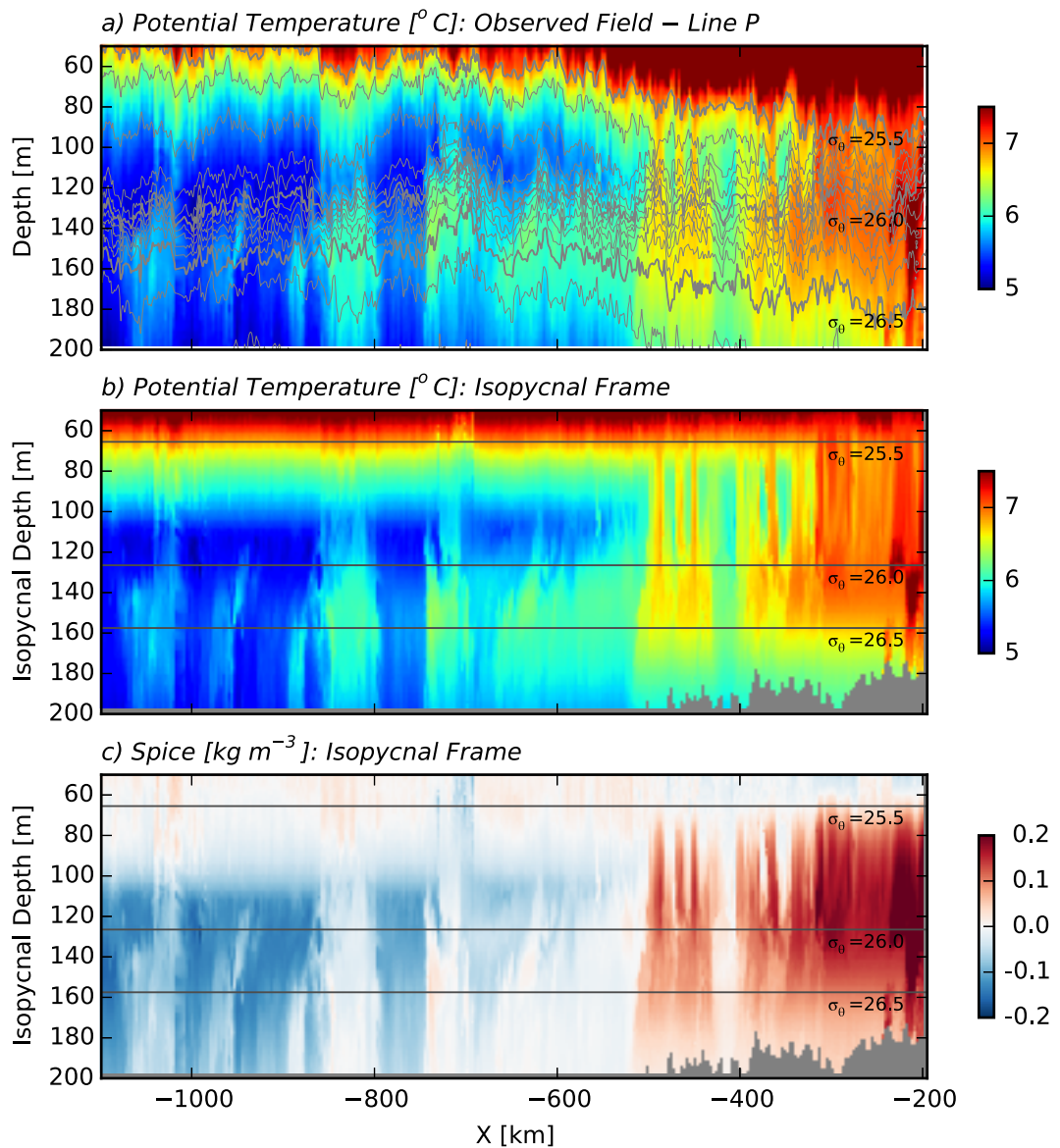


Figure 4. Temperature along Line P (a) in physical space with isopycnals contoured in black and gray. (b) Temperature along isopycnals plotted at the mean depth of the isopycnals. (c) Spice, γ , plotted on isopycnal depths. The coordinate system is distance offshore.

There are coherent structures visible in the spice field of the IWAP line (Figure 7c), but the vertical coherence is less visually pronounced than for Line P. Water to the south tends to be warmer and saltier than to the north, with the greatest contrast on the isopycnals shallower than 200 m. There are some structures that appear coherent along sloped surfaces (e.g., at $x=450$ and 480 km), similar to those observed by Cole and Rudnick [2012].

Velocity data along the IWAP section (Figure 9) is dominated by low-vertical-mode tides and higher mode inertial waves (Pickering et al., manuscript in preparation, 2015). Care has to be taken with this data set in interpreting lateral spectra because there are several gaps when the ship stopped, leading to sudden jumps in the velocity in x because the sections were not entirely synoptic (e.g., at $x = 1000$ km). The analysis below avoids these gaps.

4. Internal Waves

The internal-wave climate is not our focus, but the sections are influenced by internal waves, with isopycnal surfaces heaved by up to 50 m in some locations. We want to remove this signal by looking along

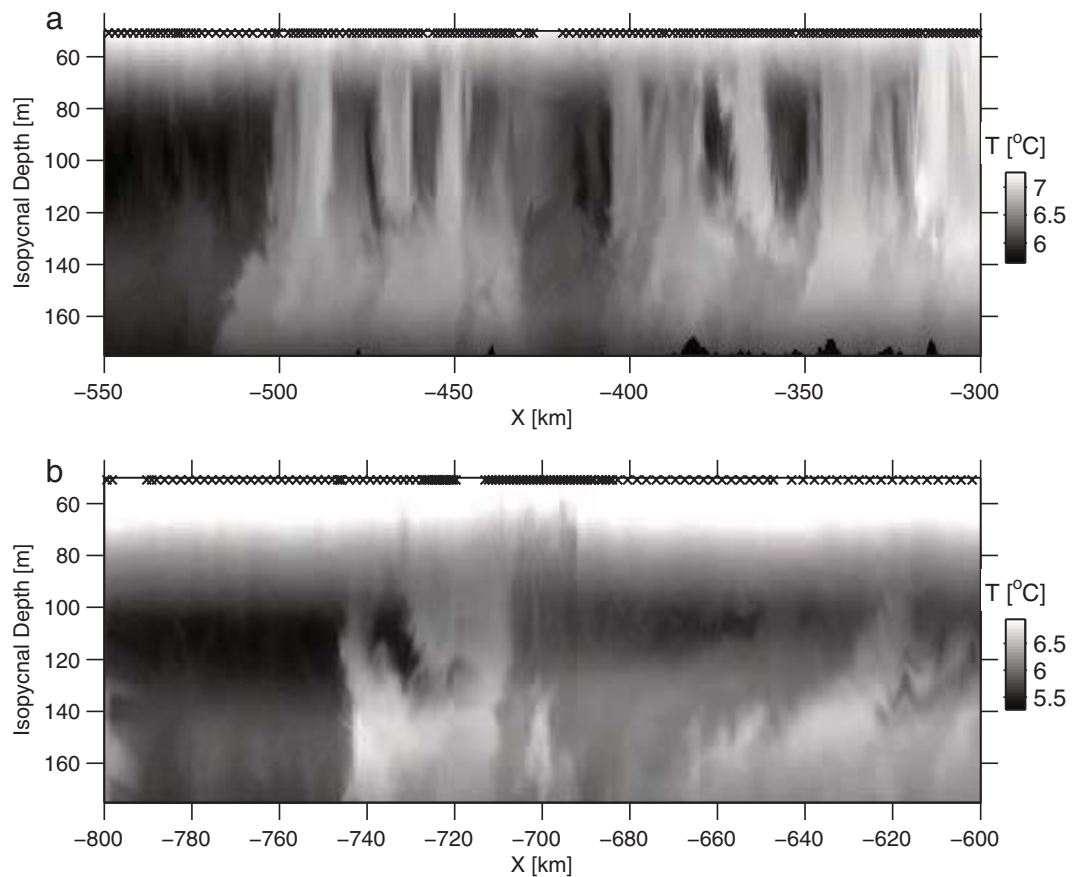


Figure 5. Details of Figure 4b showing the eddy-like structure along the warm front. The marks at the top indicate the location of MVP drops, with occasional gaps due to ship drift during a hydrographic cast.

isopycnals, but we also want to use the signal to help give us some idea of the high-wave number roll-off due to the sampling by our profilers. As shown below, the isopycnal heave follows the internal wave spec-

trum proposed by Garrett and Munk [1972] to about 3 km wavelength ($\lambda_x = k_x^{-1}$, where k_x is in cycles per km); variance lost at smaller scales can be corrected using the procedure outlined in the Appendix A.

Isopycnal heave is a useful measure of internal wave variance. The vertical displacement of an isopycnal is defined here as its distance from the section-mean depth of the isopycnal $\zeta = z(\rho) - \bar{z}(\rho)$ (this is often linearized as $\zeta = (\frac{\partial p}{\partial z})^{-1} (\rho - \bar{\rho})$, but this is no easier to compute than simply interpolating). No attempt is made to high pass the displacement, so this displacement includes large-scale isopycnal depth changes.

For the sections, care needs to be taken with the high-wave number portion of the wavefield at scales smaller than

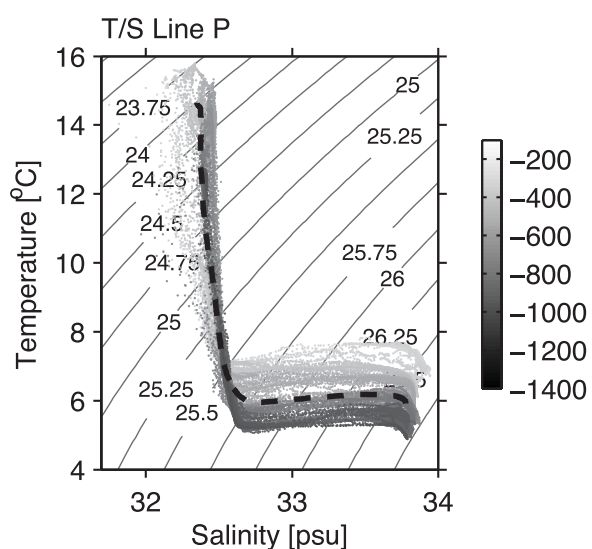


Figure 6. Temperature-salinity plot from Line P. Gray indicates distance along the line, with darker gray indicating furthest from shore. Black curve is the mean for the section used to calculate splice along isopycnals. Contours are potential density relative to the sea surface (kg m^{-3}).

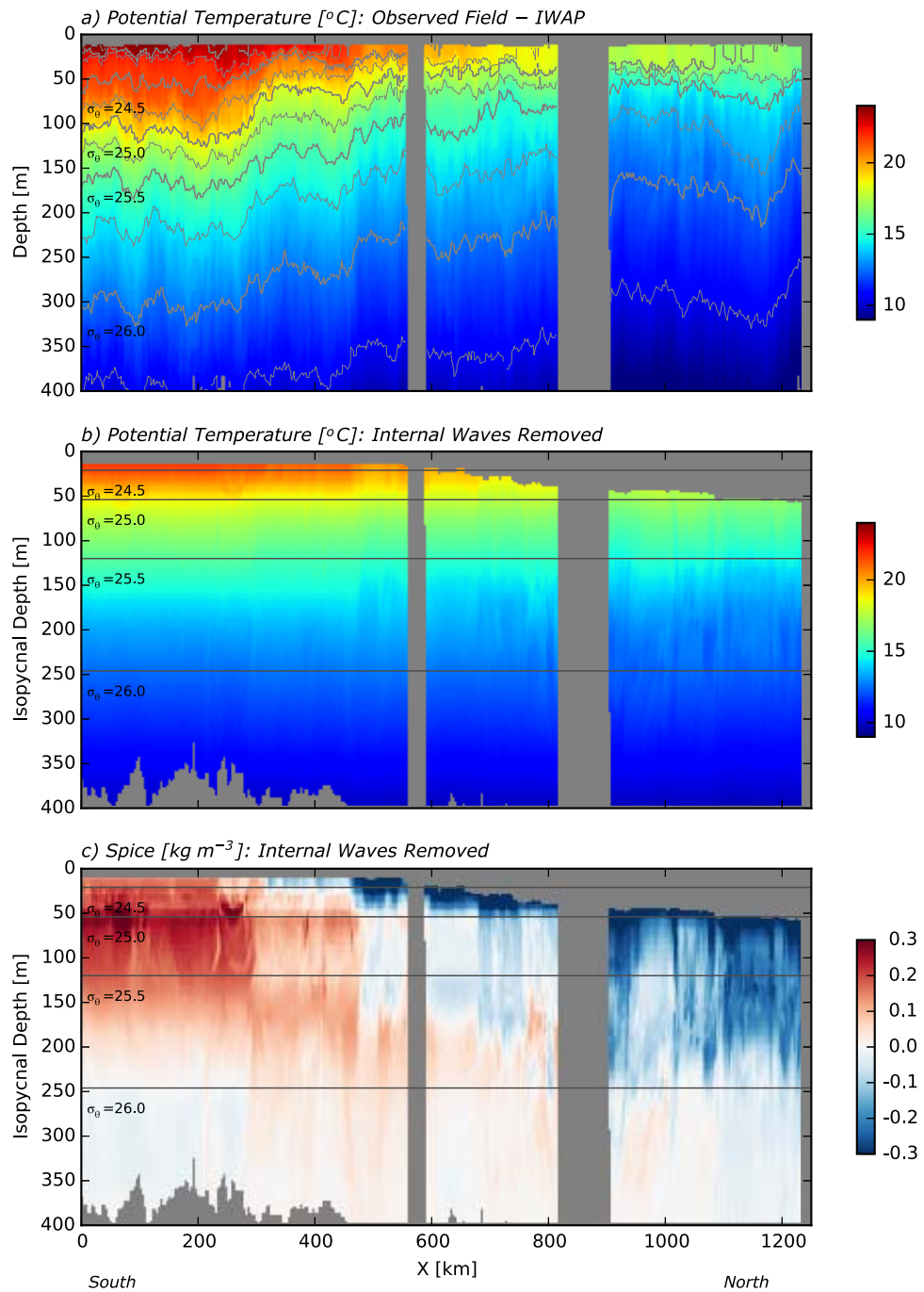


Figure 7. IWAP CTD section. Two gaps were introduced by bad weather. (a) Observed field of temperature, with isopycnals plotted every 0.25 kg m^{-3} in gray and black. (b) Temperature along isopycnals, replotted at the mean depth of the isopycnals. (c) Spice, γ , plotted along isopycnals.

10 km, which is on the order of the lateral distance between casts (median spacing $\approx 1.7 \text{ km}$ for Line P). Because casts were not evenly spaced, we linearly interpolated onto a 500 m lateral grid. Spectra were computed in 1 m depth bins and then averaged between 50 and 180 m, avoiding the surface layer and the deepest depths where the isopycnals did not span the whole line (Figure 10).

Over much of the wave number range, the displacement spectrum agrees quite well with the canonical [Garrett and Munk, 1972, GM] displacement spectrum, using the parameters as specified in Gregg and Kunze [1991]

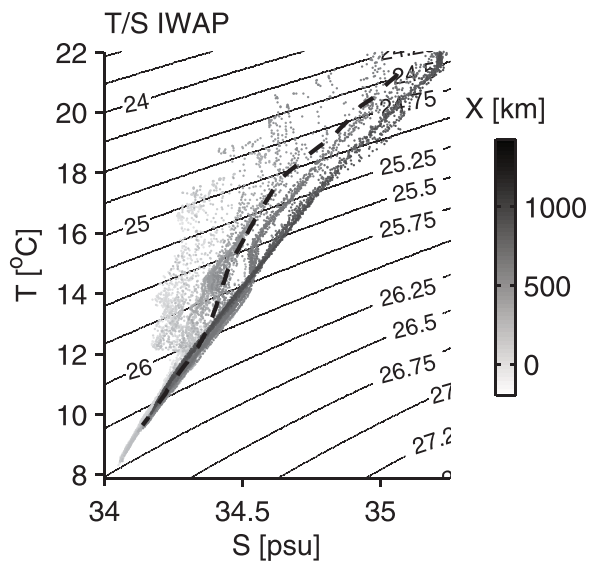


Figure 8. Temperature-salinity relation along the IWAP line. Black curve is the mean T/S curve for the whole section, averaged along isopycnals. Shaded dots are individual casts, with lighter gray being further south, and darker further north along the line. Black contours are potential density relative to pressure = 0 dbar.

working on the Line P cruise, so we cannot assess the internal wavefield from velocity.

Internal waves along the IWAP line were 1.5 times more energetic than the canonical Garrett-Munk energy level, which is expected given that the experiment was sited to investigate the fate of internal tide energy radiating from Hawaii [Alford *et al.*, 2007]. Kinetic energy was estimated from the ADCP and potential energy from the isopycnal displacements measured by SeaSoar. Here WKB-normalized spectra $\frac{N_0}{N} \phi_{PE} = \frac{N_0}{N} \frac{1}{2} N^2 \phi_\zeta$

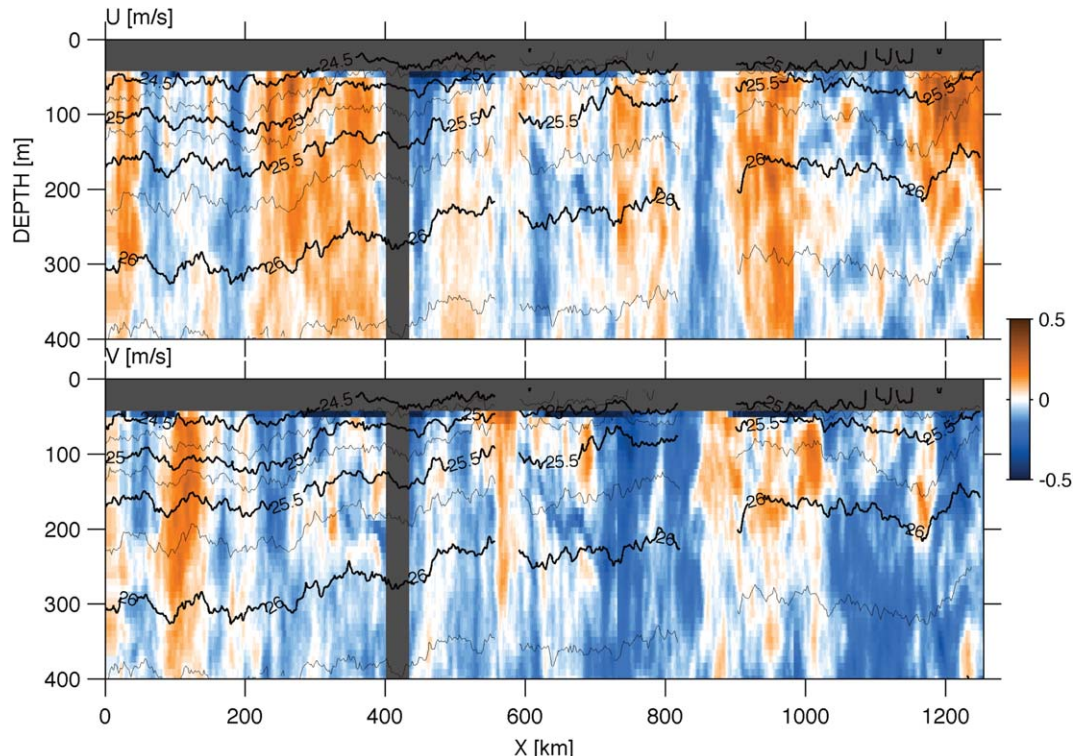


Figure 9. East-west (U) and North-south (V) velocities along the IWAP line in the upper 400 m, with potential density contours.

(other choices of the internal wave fit parameters, such as critical mode number and the exact form of the wave number dependence give similar lateral spectra); note that the amplitude of the GM spectrum has not been adjusted to fit the data. At scales smaller than 5 km, the spectrum rolls off due to the lateral sampling resolution as shown in the Appendix A. If we correct for the sampling, we get better agreement with GM at higher wave numbers (gray line).

At wave numbers below 1/50 cpkm, the spectrum of vertical displacements rises above the internal wave spectrum. If we assume a k_x^0 slope for the gradient of low-wave number vertical displacements and add this to the Garrett-Munk spectrum, there is a good agreement (Figure 10, dashed line).

Unfortunately, the acoustic Doppler current profiler (ADCP) on the ship was not

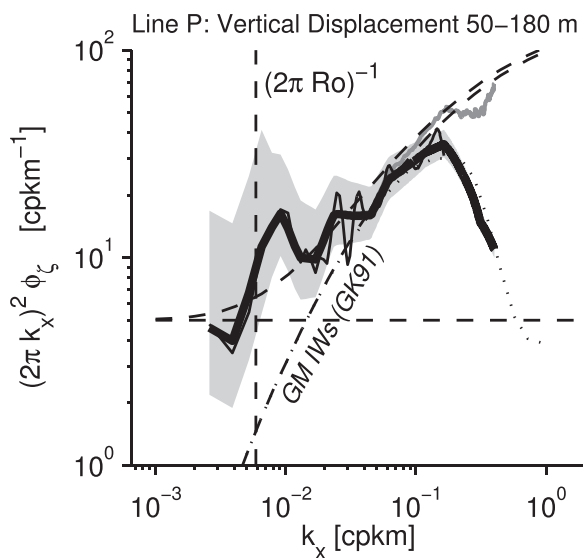


Figure 10. Lateral spectrum of vertical displacement for Line P (black line) with 95% confidence intervals shaded in gray. The spectrum is whitened by multiplying by $(2\pi k_x)^2$, and is a vertical average of spectra from different depths normalized by N_0/N . The mode-1 internal Rossby radius of deformation is indicated with the vertical dashed line. The Garrett and Munk internal wave spectrum is indicated by a curved dashed-dot line [Garrett and Munk, 1972; Gregg and Kunze, 1991]. The GM spectrum added to a red “mesoscale” spectrum is shown as a dashed line. The gray line is corrected for the response of the lateral sampling (see Appendix A). The light dotted line is the Garrett and Munk spectrum with the same sampling as the MVP.

the sampling pattern is applied, our spectra agree with the canonical spectrum. At low ($<1/50$ cpkm) wave numbers, we see an excess of energy relative to GM, similar to what we found for Line P, and the ratio of the KE to PE of this energy is approximately 2.

5. Spice Statistics

Here we present statistics based on the spice signals to help understand the nature of the lateral stirring. In addition to spectra, we will consider the lateral displacements along isopycnals implied by the ordering of spice along the isopycnal, the lateral decorrelation scale, the vertical coherence scale, and histograms of lateral spice gradient. These statistics are all variable with depth and indicate that different stirring processes must be occurring due to either depth-dependent forcing or the time evolution of the tracer field in the ocean.

We have chosen to bin statistics in depth ranges and, for Line P, two lateral regimes. For Line P, we identify a change in statistics 550 km offshore that justifies separating the water influenced by the California Undercurrent from the water in the bulk of the Gulf of Alaska. Depth bins are 0–60 m for a surface layer in both data sets. Below this is the “remnant layer” of low-stratified water left over from the previous winter’s cooling, which is 60–120 m for Line P and 60–140 m for IWAP. The main thermocline is 120–170 m for Line P and 140–250 m for IWAP. A fourth depth bin is used for deeper water at the IWAP line. These depth ranges are somewhat arbitrary, but, as we see below, the statistics in each are often unique, justifying the binning.

5.1. Lateral Displacements

A diagnostic, borrowed from the three-dimensional turbulence literature [Thorpe, 1977], is to imagine that an isopycnal spice section reflects small-scale variability from stirring processes superimposed on larger-scale monotonic spice gradients. Resorting a section such as that shown in Figure 12 to be monotonically decreasing offshore gives a rough estimate of how far each parcel has been stirred from its “original” location. Such a 1-D sorting procedure imagines that interleaving of water happens along the line, which is almost certainly not the case, but nonetheless provides a measure of how far each water parcel would have to be displaced laterally to give the observed field, Δx .

and $\frac{N_0}{N} \phi_{KE} = \frac{N_0}{N} \frac{1}{2} (\phi_U + \phi_V)$ are averaged from 500 km long lateral windows at each depth, and corrected for the sampling from the ADCP and SeaSoar (Figure 11a). The resulting averaged spectra have a shape similar to the GM shape at high wave numbers, and more variance than GM at low wave numbers, as for Line P. At high wave numbers, the ratio between kinetic energy and potential energy is 3, as in the GM model. At lower wave numbers, APE and HKE are closer in energy level. The flattening at low wave numbers is perhaps related to mesoscale motions or near- M_2 waves dominating these scales, with a KE/PE ratio closer to the frequency-dependent M_2 value of 2.6.

Callies and Ferrari [2013] present similar spectra from the SPICE experiment in the North Pacific. Their kinetic energy spectra are considerably redder than ours at high wave number, but they point out this may be due to interpolation onto a regular grid, which they do not correct for. When a correction for

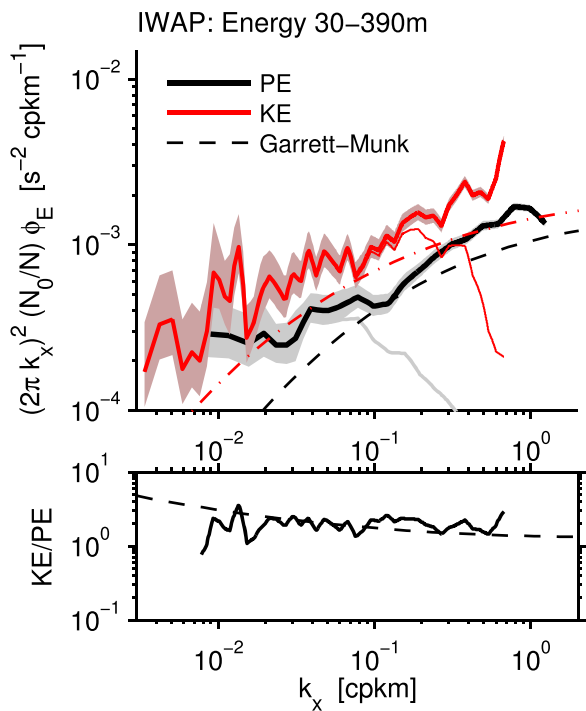


Figure 11. (a) Energy spectrum from IWAP; potential energy (PE) is derived from the displacement of isopycnals as measured from the SeaSoar; kinetic energy (KE) from the ship's Doppler profiler. Spectra have been normalized for stratification, and whitened by multiplying by $(2\pi k_x)^2$ for presentation purposes. The spectra are corrected at high wave numbers for SeaSoar's and the Doppler profiler's sampling using the empirical model as described in the Appendix A. The raw spectra without this correction are shown as thin lines. The dashed lines are the Garrett-Munk model. (b) Ratio of kinetic energy to potential energy, observed (solid) and Garrett-Munk model (dashed).

bins exhibit wider distributions than onshore observations. We interpret the wider, asymmetric distributions as indicative of sporadic stirring, whereas tight symmetric distributions imply more complete and homogeneous stirring. Along Line P, lateral displacements become smaller with depth. Conversely, the IWAP data shows the opposite trend in the lateral displacements, with larger deep displacements than closer to the surface. This indicates that these lateral mixing regimes are likely quite different.

If we assume that the ship path is perpendicular to mean lateral gradients, which is a good approximation for these ship tracks (Figure 2), then the standard deviation of the lateral displacements can be related to a turbulent length scale, $L = \text{std}(\Delta x')$. If we assume a time scale over which the stirring took place, T , then we can infer a lateral diffusivity via $\kappa_H \sim L^2/T$. For the shallow and remnant layers, a time scale on the order of the time since spring restratification seems appropriate, so $T \approx 120$ days for Line P, and $T \approx 90$ days for IWAP.

The inferred lateral diffusivities this very rough estimate provides (Figure 14) are in reasonable agreement with the lateral along-isopycnal diffusivity of $K_H \approx 2000–3000 \text{ m}^2 \text{s}^{-1}$ derived from floats for this region [Zhurbas and Oh, 2003], though there is clear depth dependence. The depth dependence likely represents incorrect estimates for the time over which the stirring might have occurred. For the shallow and remnant layers, we are supposing that there is a seasonality to the input of scalar variance and lateral stirring that has not been clearly demonstrated to our knowledge. For the deeper layers, there is no reason to think lateral gradients were reset recently, and applying the seasonal stirring time scale is inappropriate.

5.2. Lateral Decorrelation Length Scales

The decorrelation length scales of spice along an isopycnal are another measure of turbulent stirring, and are more directly comparable to the Lagrangian decorrelation scales derived from floats than the “displacement” scale in the previous section. The decorrelation length scales are significantly shorter than these

The example trace from Line P shows the two basic regimes (Figure 12): a region of steep large-scale spice gradient onshore of $x = -550$ km and a shallow-gradient region offshore. There are large displacements, Δx , in the offshore part of the section where intermittent lenses of warm water punctuate the cooler offshore waters (Figure 12b).

These two regimes can be differentiated statistically by considering histograms of inferred lateral displacements (Figure 13). Raw histograms of Δx are dominated by the large-scale displacements in Figure 12b, which are likely indicative of large-scale stirring. To diagnose the smaller-scale stirring, we high pass this signal to remove the variability at scales larger than 200 km and plot the deviation $\Delta x'$ (Figure 12c).

Onshore of $x = -550$ km, the Line P data show strong differences with depth, with the near-surface layer having much larger lateral displacements than the deeper layers (Figure 14a). A similar trend is seen offshore (Figure 14b), though all three depth

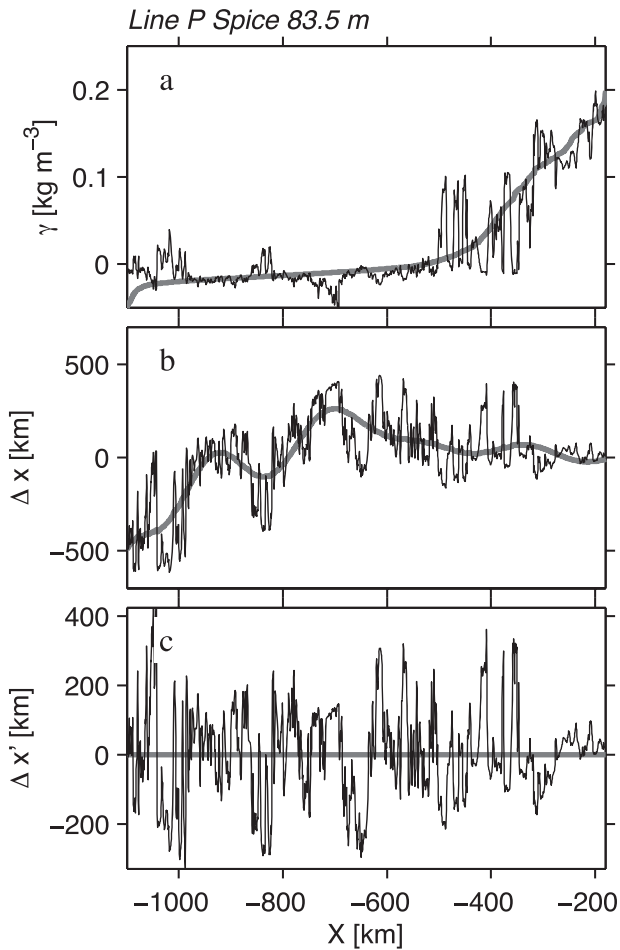


Figure 12. (a) Spice along Line P at 83.5 m mean-isopycnal depth. Thick line is the sorted version of the spice. (b) Lateral displacement of spice at 83.5 m depth along Line P that would reorder the observed spice to monotonically decreasing offshore. The thick line is the low-pass trend removed to get (c) the high-passed lateral displacements.

associated with this lateral structure, so we cannot use this information to corroborate our estimates of diffusivities. Zhurbas and Oh [2003] indicate that the time scale will be on the order of three days, which means tracking the evolution of small-scale features of this flow using Eulerian snapshots would be challenging.

5.3. Spice Spectra

The shape of gradient-tracer spectra can indicate what physical processes are stirring the tracer. From the sections of spice shown above, it is clear that the spectra are generally red and that the deeper spectra are redder than the shallow spectra (Figure 16). As pointed out in section 1, we have whitened the spectra by multiplying by the horizontal wave number $(2\pi k_x)^2$ and normalized by the large-scale spice gradient, $d\gamma/dx$ over the length analyzed for each spectral block. Thus, a k_x^{-2} tracer-variance spectra will appear as a k_x^0 tracer-gradient spectra, and a bluer k_x^{-1} tracer-variance spectrum predicted by QG/SQG away from the surface would appear as a k_x^1 tracer-gradient spectrum. As discussed, we whiten the spectra to make the difference between slopes clearer by eye. Spectra are calculated at each depth in 50% overlapping 200 km long Hanning-windowed bins, then averaged in depth bins, and smoothed logarithmically in wave number. The raw spectra roll-off at high wave numbers (Figure 16, thin lines), so we apply a correction for variance lost due to horizontal gridding (Figure 16, thick lines), and truncate our spectra at 0.3 cpkm (see the Appendix A). Confidence intervals are determined from a chi-squared distribution for which the degrees of freedom are computed from the number of overlaps in the windowed segments, the number of smoothed wave number bins, and the number of independent spectra averaged in each depth bin. The number of

"displacements," and are thought to reflect the size of eddies stirring the fluid [e.g., LaCasce, 2008]. We calculate the lag correlation on each isopycnal from the high-passed spice signal in order to avoid correlation due to the background gradient of scales larger than 200 km (Figure 15). If we define the decorrelation length scale as where the lag correlation is first less than 0.1, length scales are similar to the local mode-1 Rossby radius of deformation [Chelton et al., 1998], $R \sim 30$ km (Figure 15; $R=c/f$, where c is the mode-1 wave speed, and f the local Coriolis frequency).

The calculated decorrelation scales are broadly consistent with the results from float trajectories compiled by Zhurbas and Oh [2003]. In those studies, the observed Lagrangian length scale is about 20 km at Line P, and about 25 km at IWAP. This indicates that the decorrelations observed by our Eulerian measurements are similar to Lagrangian estimates. We do not have an estimate of the time scales

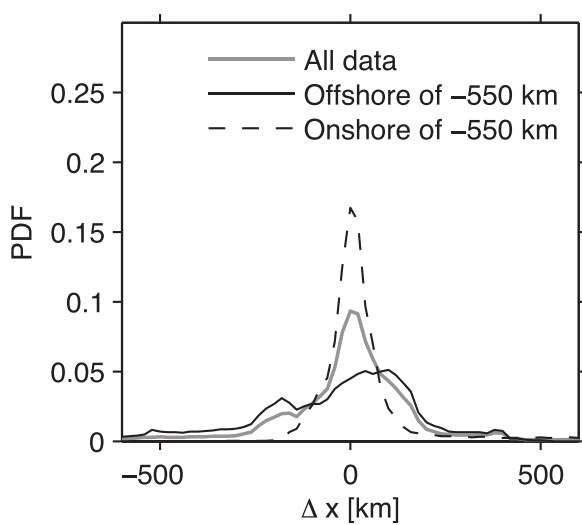


Figure 13. Line P probability distribution function of lateral displacement, Δx , deeper than 60 m, and offshore of $x = -550$ km (solid), onshore of $x = -550$ km (dashed), and all the data (gray).

features seen in the sections above. Fitting a power law to these spectra is also somewhat dependent on the wave number range chosen. However, the deeper Line P tracer-gradient spectra clearly become redder (less high-wave number variance) with depth, with power laws k_x^{+1} to k_x^0 . This is the opposite of the depth trend predicted by QG/SQG theory (Figure 1).

Spice spectra along isopycnals are similar at all depths on the IWAP line, with slopes roughly consistent with $k_x^{1/3}$ (Figures 16g–16j). The portion of the spectra being corrected for lost variance due to the sampling is above 0.1 cpkm.

Except for the surface depth bin along Line P, the spectra here are all redder than the k_x^1 predicted from QG/SQG theories though not as red as k_x^0 , except for the deepest Line P spectra. The spectra here are variable, but consistently bluer than k_x^0 , and show increasing redness with depth in some cases.

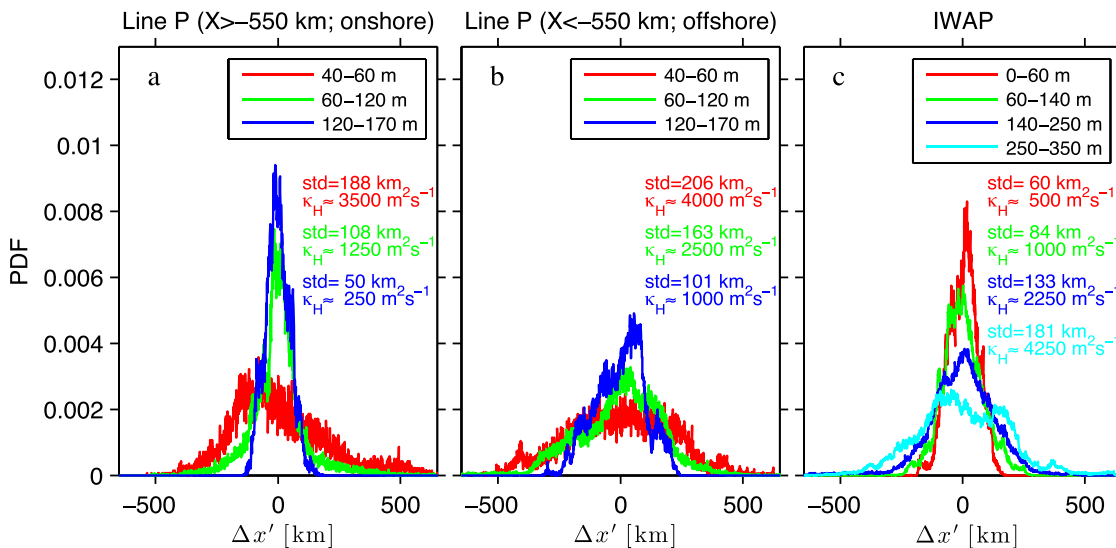


Figure 14. Probability density functions of high-passed lateral displacement, $\Delta x'$: (a) for Line P onshore of $x = -550$ km, (b) for Line P offshore of $x = -550$ km, and (c) for IWAP. Three depth bins are indicated for Line P, four for IWAP. The standard deviation of each data set is indicated. A rough diffusivity estimate is also presented, assuming that diffusivity is $\text{var}(\Delta x')/T$, where $T = 120$ days for Line P, and $T = 90$ days for IWAP, both chosen to be the time since spring restratification.

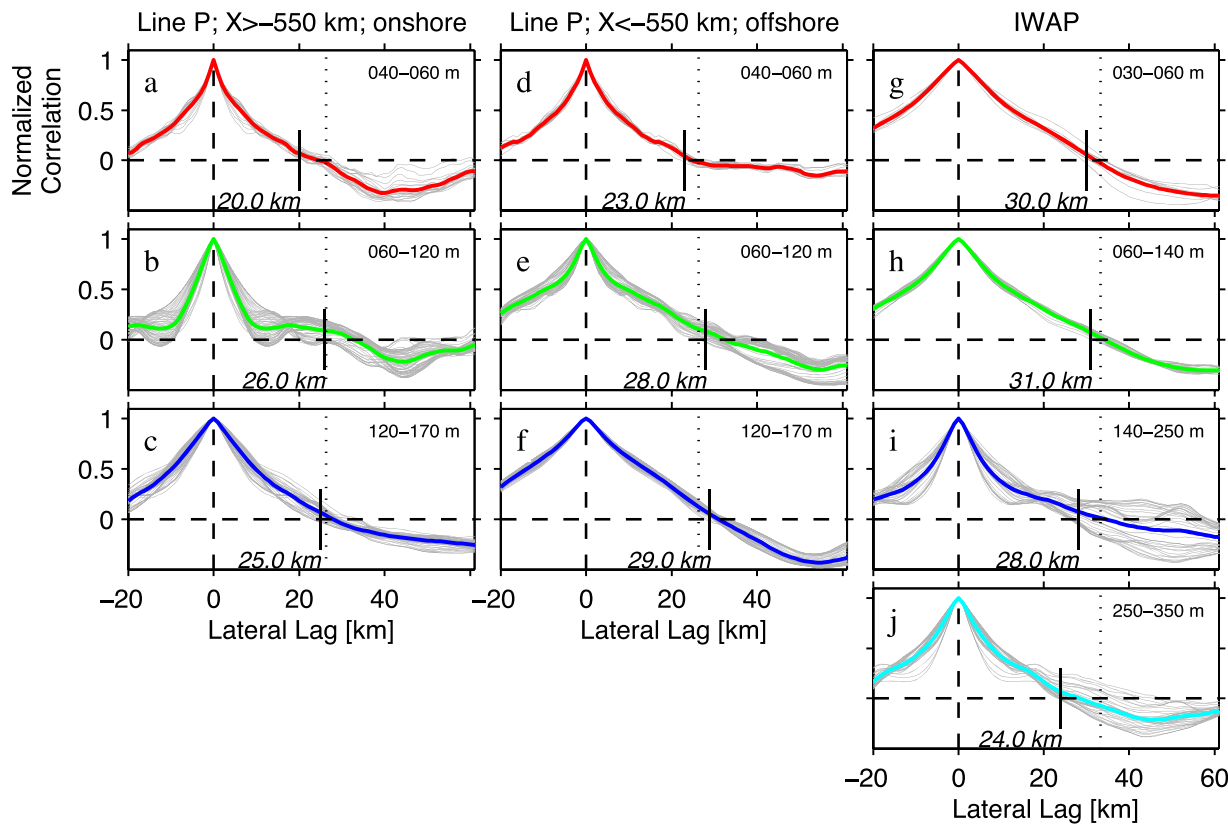


Figure 15. Lateral lag correlations for high-passed ($\lambda < 200$ km) spice along isopycnals for the two data sets. Individual traces are in gray, and the average for the space/depth bin is colored. The short vertical black line indicates the decorrelation scale, defined as when the mean trace first drops below a lag correlation of 0.1. The dotted vertical lines are the local Rossby radius of deformation.

5.4. Vertical Coherence

The nature of the lateral stirring will affect the vertical coherence of the spice signal, though this metric is not directly reported in theory or modeling studies that we have seen. *Smith and Ferrari* [2009] report 2-D spectra, which will have the same information. Stirring by low-mode eddies is expected to produce depth-correlated scalar spectra, as is seen in QG models of stirring by geostrophically balanced mesoscale motions [see *Smith and Ferrari*, 2009, Figure 17]. We cannot carry out a meaningful two-dimensional spectral estimate with data that only extend 200 or 400 m deep, so we estimate the depth correlation from the data sets by calculating coherence squared of a reference isopycnal depth z_0 and comparing it to all other isopycnal depths z

$$C^2(z_0, z, k_x) = \frac{\langle |P(z_0, k_x)P^*(z, k_x)|^2 \rangle}{\langle |P(z_0, k_x)|^2 \rangle \langle |P(z, k_x)|^2 \rangle}, \quad (2)$$

where $P(z, k)$ is Fourier transform at depth z . For any given depth, z_0 , this coherence depends on depth z , and drops as $|z_0 - z|$ gets larger (Figure 17). The angle brackets represent the averaging over 50% overlapping 100 km Hanning windowed spectral estimates. The vertical decorrelation length scale, $\Delta = (\Delta_{up} + \Delta_{dn})/2$, is defined as the average distance above and below z_0 (Δ_{up} and Δ_{dn} , respectively) that the coherence drops below 0.75 (red curve, Figure 17).

Calculating $\Delta(z, k_x)$ at all isopycnal depths shows that coherence of the spice signal depends on the horizontal wavelength, and that there are distinct depth regimes (Figure 18) where the correlation scale is larger. For instance, onshore at Line P ($x > -550$ km), the correlation scale reaches 40 m or more at $k_x = 100^{-1}$ cpkm centered at the 100 m isopycnal depth, where the coherent spice features are found (40 m implies the features are about 80 m tall, as in Figure 4). Further offshore ($x < -550$ km), near-surface and deeper layers have larger vertical correlation than middepths. The IWAP data have shorter length scales, with a maximum of about 20 m (Figures 18e and 18f) and the depth dependence is less pronounced than along Line P.

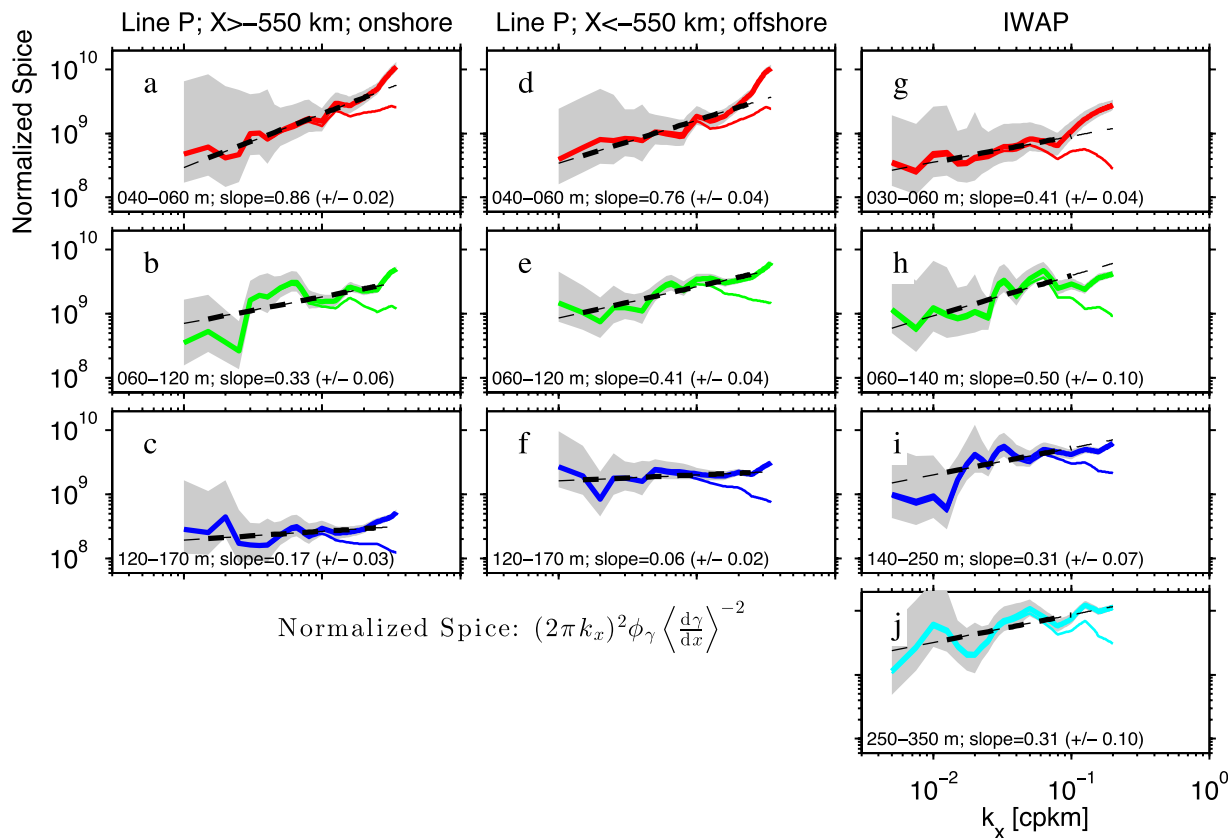


Figure 16. Spectra of lateral spice variations, normalized by the large-scale spice gradient. The gray bars are confidence intervals calculated as discussed in the text. The dashed line is the power law fit, the results of which are indicated at the bottom of each panel. Uncertainties in the slope are from uncertainties in the linear regression, which is weighted by the degrees of freedom of each spectral estimate.

Both data sets show larger vertical coherence scales at lower wave numbers with power laws of $k_x^{-0.4}$ to $k_x^{-0.85}$ (Figures 18b, 18d, and 18f). There is an indication from taking longer coherence estimates that the vertical coherence scale saturates at around 20 m at horizontal scales larger than 100 km, but the statistics on these estimates are poor (Figure 18f).

These scales are small compared to the ocean depth, as expected from looking at the raw data. This lack of large-scale coherence in the vertical is unexpected if the ocean is being stirred by low-mode motions. Cole and Rudnick [2012] use empirical orthogonal functions (EOFs) to demonstrate that layers approximately 100 m thick are uncorrelated over a section, a similar conclusion to what we find here for the lowest wave numbers. The analysis here extends those findings to show the fall-off of vertical coherence with horizontal wave number in a relatively consistent manner across both data sets. Todd *et al.* [2012] also argue that there are layers of spice variance in the California Current system off the California coast, but posit that these are largely due to differences in the surface setting the strength of spice gradients. The coherence analysis used here does not care about the strength of the spice gradients, just whether they are coherent or not. The lack of vertical coherence between different depths, even at large horizontal length scales implies that the stirring of those isopycnals is different, either in strength or in history.

5.5. Probability Distribution of Lateral Gradients

One explanation given for redder (less high- k_x variance) passive tracer spectra than predicted from QG theories is that stirring motions create frontal structures in the flows Klein *et al.* [2008] and Capet *et al.* [2008]. Fronts imply large regions of homogenous tracer ($d\gamma/dx$ is small) interspersed with occasional instances of large gradients ($|d\gamma/dx|$ is large). Conversely, a naive model for a random tracer field with whitened spectrum of k_x^0 would be a normal (Gaussian) distribution of tracer gradients. The observed probability density functions (PDFs) of $d\gamma/dx$ are considerably more peaked than a normal distribution (Figure 19) with large values of kurtosis, consistent with fronts.

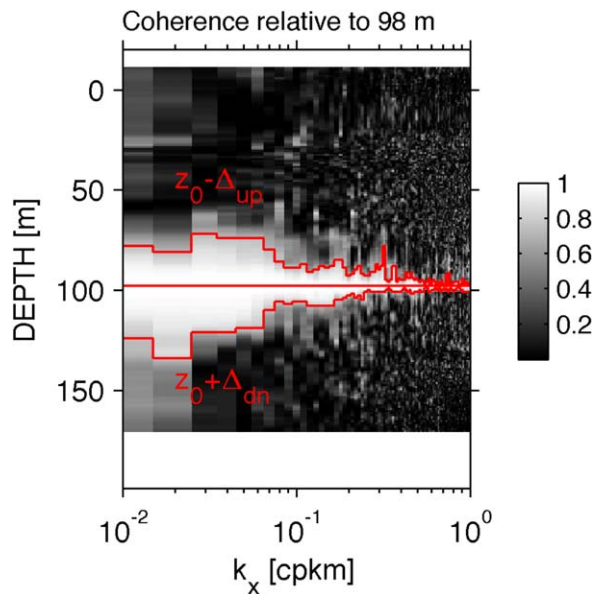


Figure 17. Line P: contour of coherence squared between the spice signal at $z_0 = 98$ m (red horizontal line) and all other isopycnal depths in the section. Coherence decreases with distance, and we define $z_0 - \Delta_{up}$ and $z_0 + \Delta_{dn}$ as the depth where the coherence drops to less than 0.75 (red lines).

IWAP are more varied (Figures 19g–19j), with very large kurtosis in the three shallowest bins, and moderate kurtosis in the deepest. The spectra for IWAP vary little in these depth bins and there is no clear correlation with the PDFs. Like offshore Line P, these distributions are more consistent with fronts near the surface, but differences are small. Also, compared to Line P, the IWAP data have much higher kurtosis, perhaps indicating frontogenesis is more prevalent along the IWAP line.

Finally, all the distributions have essentially zero skewness, indicating that the high-wave number variability is relatively isotropic and that fronts are created in the large-scale up and down-gradient directions in equal proportions.

6. Summary and Discussion

6.1. Internal Waves and Submesoscale Motions

For the two locations considered here, internal waves dominate vertical displacements of isopycnals in the submesoscale (<20 km) part of the spectra. The shapes and amplitudes of the spectra are very close to the canonical internal wave spectrum [Munk, 1981; Gregg and Kunze, 1991]. At lower wave numbers (1/500 cpkm for Line P, and 1/200 cpkm for IWAP), the isopycnal displacements become more red, and reach a slope close to k_x^{-2} .

Similarly, the kinetic energy spectrum for IWAP follows the canonical internal wave shape over the scales we measured, with a hint of low-wave number enhancement suggestive of a mesoscale-and-larger velocity field. The internal waves appear to be slightly more energetic than canonical Garrett and Munk level (GM), consistent with observations of a strong near-inertial signal at these latitudes (Pickering et al., manuscript in preparation, 2015). The ratio of kinetic to potential energy is 3, consistent with GM, except at the lowest horizontal wave numbers, where it asymptotes to something close to the M_2 tidal ratio of 2.6. Whether these lower wave number features are primarily internal waves or mesoscale motions is impossible to determine from this data set.

As found by Callies and Ferrari [2013], it is difficult to pick out “submesoscale” features from the velocity or displacement signals in the eastern North Pacific due to the dominance of internal waves. Callies and Ferrari [2013] found more robust results closer to the Gulf Stream. However, it would be helpful if results for passive tracers were presented regularly in the theoretical and modeling literature, since passive tracers along isopycnals are far less affected by internal waves.

As with the spectra, there are significant differences in the PDFs of $d\gamma/dx$ with depth and space. For Line P, onshore of $x = -550$ km (Figures 19a–19c), the near-surface water has many large gradients but only weak peakedness. It also has the bluest spectrum (Figure 16a). Conversely, the deepest bin, which also had the reddest spectrum close to k_x^0 , has the largest kurtosis; the middle bin (60–120 m) is intermediate. Offshore (Figures 19d–19f) the opposite trend occurs, with higher kurtosis near the surface, and decreasing at depth. Thus, onshore at Line P, the character of the tracer distribution is more “front-like” for the deeper bins, and less so for the shallower, which is opposite of what we would expect if surface frontogenesis was responsible for the observations.

The probability distributions from

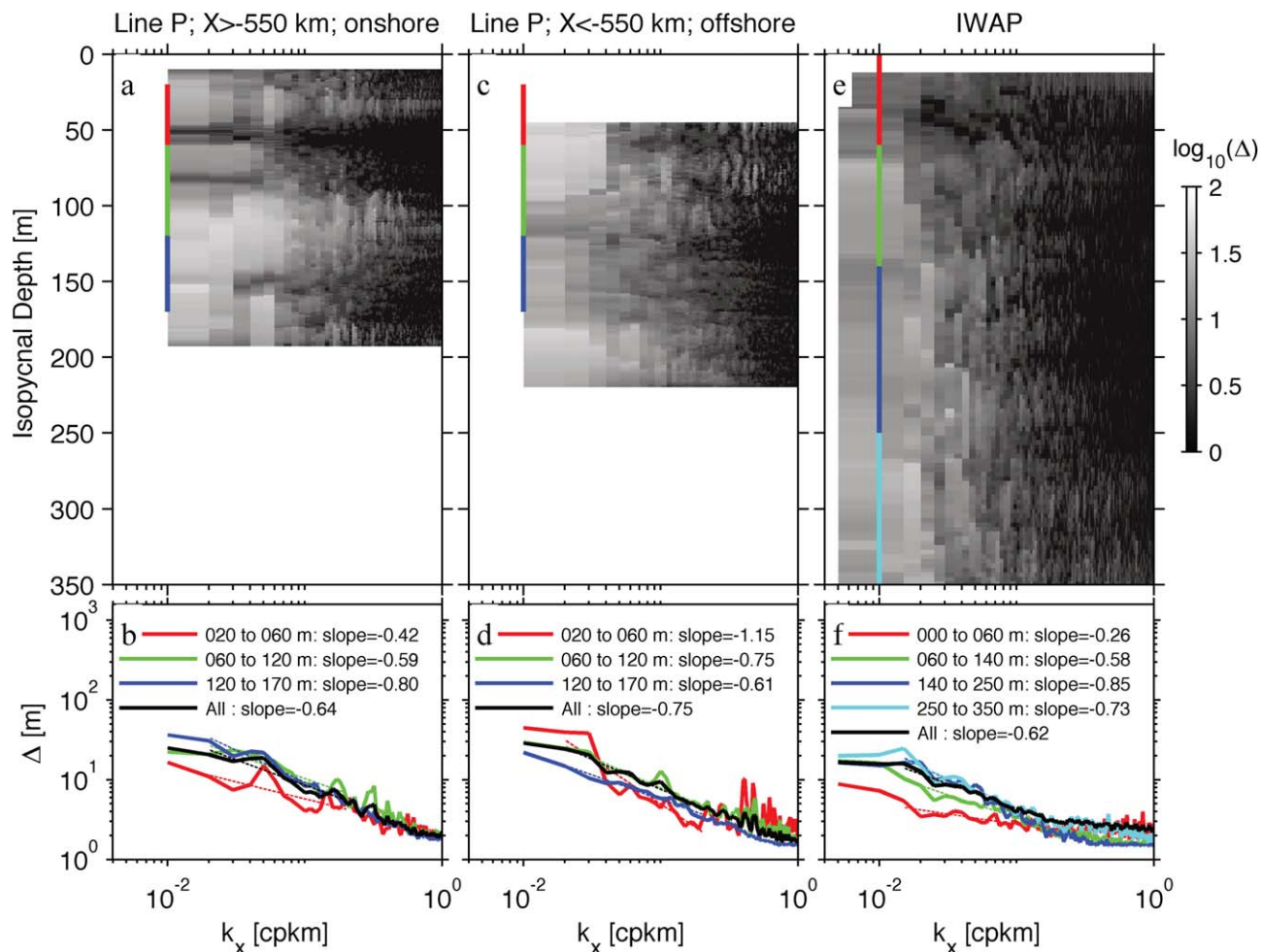


Figure 18. Vertical decoherence scales as functions of horizontal wave number. (a, c, and e) The scale Δ over which the vertical decoherence drops to less 0.75 for each depth bin in the data set. Colors on left indicate depth bins over which the averaging took place. (b, d, and f) The average of Δ as a function of k_x in each depth bin (colors) and the full depth average (black). A power law fit is indicated for each average, fit to wave numbers less than $k_x < 1/50$ cpkm.

6.2. Spice Signals and Lateral Stirring

Our analysis of the spice along isopycnals indicates significant spatial dependence independent of the strength of the large-scale gradient:

1. There are lateral regimes, particularly in the Line P data set, where the spectral shapes are not very different, but the degree of lateral stirring is, as evidenced by very different histograms of the lateral displacements (Figure 14).
2. Decorrelation scales are essentially the same in the Eulerian spice properties as they are in Lagrangian float trajectories (Figure 15). It is not obvious that this should be the case, and we think is an interesting finding.
3. There are layers of spice coherence, approximately 100 m thick, but not thicker, indicative of different stirring histories or depth-dependence to the stirring mechanisms between the layers, and arguing against their being stirred in situ by the same physics.
4. The spectra become redder with depth for the Line P data (Figure 16), the opposite of what would be expected for near-surface frontogenesis, and perhaps indicating nonlinear motions input in the main thermocline via baroclinic instability of the California Undercurrent. This reddening of the spectra with depth was not apparent in the more open-ocean IWAP data.
5. The spice gradients have high kurtosis probability distributions, implying low-gradient regions punctuated by high gradients, as one would expect for a front-dominated signal. Along Line-P the peakedness *increases* with depth, again implying that near-surface processes are not directly responsible for the observations.

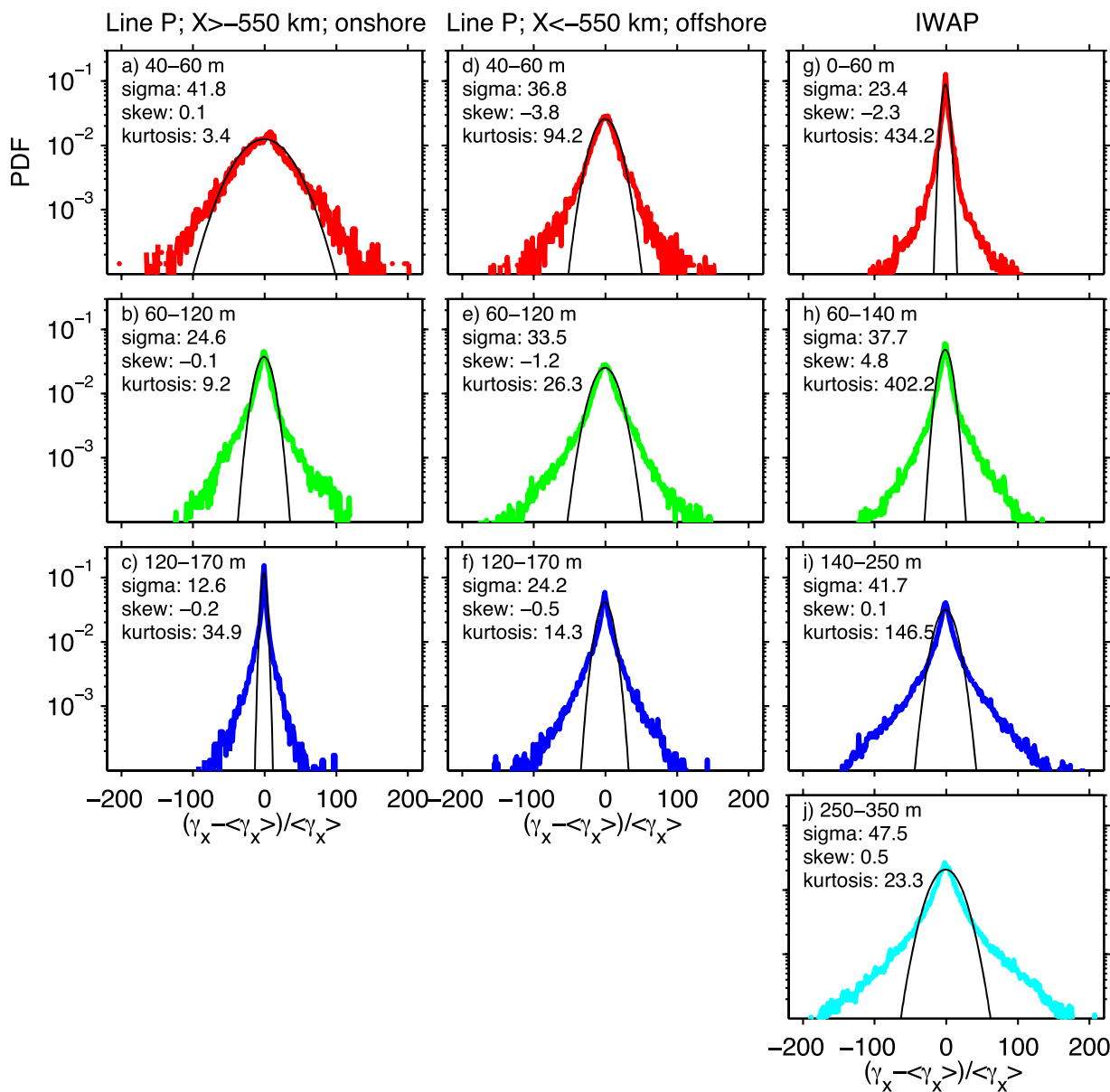


Figure 19. Histograms of normalized spice gradients in spatial bins. A normal distribution is fit to the data for comparison, and the statistics derived from the moments of the distribution indicated.

Our lowest order results are in agreement with previous efforts, in that we find that lateral spectra of tracer variance are redder (less high- k_x variance) than predicted by quasi-geostrophic theories (Figure 16 and Table 1, fourth column). However, our results indicate that the tracer spectra are usually not as red as k_x^0 with only the deepest spectra at Line P having such red slopes; most of our spectra were closer to $k_x^{1/2}$ to $k_x^{1/3}$ at our locations, and dissipation of lateral variance is presumably more vigorous than predicted by low-mode QG/SQG, but not as red as would be expected from pure frontogenesis [Boyd, 1992].

The reason behind this is not readily evident. There is evidence that the tracer distributions are more peaked than a normal distribution (Figure 19 and Table 1, last column), lending some evidence for the importance of frontal processes. However, this statistic varied with depth, and a lot from place to place, with very high kurtosis (peakiness) along IWAP and weaker at Line P. The offshore Line P data and the IWAP data behave somewhat similarly, with decreasing peakiness with depth, perhaps indicating the importance of near-surface frontogenesis offshore. Nearshore Line P may be unique in that it is near the California Undercurrent and its interaction with topography, and therefore subject to mid-depth vorticity input [Pelland et al., 2013].

Table 1. Summary of Spice Statistics Reviewed in This Paper^a

Isopycnal Depth Range	RMS Lateral Displacement (km)	Lateral Decorrelation (km)	Spectral Slope	Vertical Coherence Scale at 1/100 cpkm (m)	Kurtosis $d\gamma/dx$
<i>Line P: Onshore ($x > -550$ km)</i>					
Surface (40–60 m)	200	20	$k_x^{0.9}$	10	3
Remnant (60–120 m)	100	25	$k_x^{0.3}$	15	9
Thermocline (120–200 m)	50	25	$k_x^{0.2}$	25	35
<i>Line P: Offshore ($x < -550$ km)</i>					
Surface (40–60 m)	200	25	$k_x^{0.8}$	40	94
Remnant (60–120 m)	150	30	$k_x^{0.4}$	30	26
Thermocline (120–200 m)	100	30	$k_x^{0.1}$	25	14
<i>IWAP</i>					
Surface (0–60 m)	50	30	$k_x^{0.4}$	10	434
Remnant (60–140 m)	75	30	$k_x^{0.5}$	15	402
Thermocline (140–250 m)	150	30	$k_x^{0.3}$	20	147
Deep (250–350 m)	175	25	$k_x^{0.3}$	20	23

^aDepths are isopycnal depths.

However, we do not think surface frontogenesis or low-mode stirring are responsible for much of the variance, given that the spectra do not get bluer with depth and also because the coherence of the spectra drop off rapidly in the vertical direction (Figure 18 and Table 1, fifth column). The vertical scale at 100 km for the coherence squared to be above 0.75 is 40 m. This indicates to us independent sources of stirring at depth and possibly varying time histories for the water masses. It also indicates that flows are very low aspect ratio (1000:1), an order of magnitude flatter than aspect ratios predicted from QG theories, which predict f/N [Smith and Ferrari, 2009]. Cole and Rudnick [2012] also reported flatter aspect ratios, though not as flat as we find here (using their method, we got the same 1000:1 aspect ratio as our coherence analysis).

The power law of the vertical decoherence scale as a function of k_x is relatively robust, at something similar to $k_x^{-1/2}$. The simplest model for this structure would be $\Delta \sim K_h^{-1}$, which assumes that the spice variance has a constant aspect ratio. If it is also assumed that the coherence is isotropic in wave number space, then the same power law applies to the observed one-dimensional spectrum: $\Delta \sim k_x^{-1}$ [e.g., Callies and Ferrari, 2013]. The observed coherence falls off more slowly than what a single horizontal-to-vertical aspect ratio would indicate, and small scales are relatively more vertically coherent than large scales. We do not have an explanation for this finding, but think it merits further investigation.

The root-mean squared lateral displacement of parcels (second column of Table 1 and Figure 14) tells us something about the nature of turbulent stirring that other statistics do not. The distribution of the displacements is different for the two Line P regimes (Figure 14), with the onshore distribution being more normal, and the offshore irregular. We interpret this to mean that the spice in the onshore region is being actively stirred, whereas the offshore spice is subject to episodic intrusions of high-spice onshore water, possibly geostrophically balanced coastal eddies [Crawford, 2002] or smaller California Undercurrent eddies [Pelland et al., 2013]. IWAP has a strong depth trend to the sorting statistic (Figure 14c), with surface layers having relatively symmetrical distributions indicating homogenous stirring, whereas deep layers are more asymmetric. This asymmetry can be seen in the raw spice image for IWAP (Figure 7c) with high spice punctuating the low-spice background (e.g., at $X = 220$ or 460 km). These features are relatively coherent with depth, and appear to trace their origin back to 150 m depth or so, or the permanent thermocline. These features may originate during springtime restratification [e.g., Boccaletti et al., 2007].

The lateral diffusivities inferred from the resorting procedure are speculative since we do not know the lifetime of these coherent features or how fast they are traveling. To get out to $x=500$ km in the 120 days postulated above would require a sustained eddy speed of 0.035ms^{-1} , which is not unreasonable. Our lateral diffusivities are not unreasonable compared to surface float data [Zhurbas and Oh, 2003].

Nonstationary effects should be considered so close to the sea surface. At Line P, the “remnant” layer was the mixed layer in the winter, and has a significantly different stirring history than the deeper thermocline waters, or the well-stratified surface waters. At IWAP, subduction of deeper water from further north means

its stirring history is similarly not well determined by local dynamics. This calls for more measurements of the seasonal cycle of upper ocean spice such as those by Cole and Rudnick [2012], and hopefully more exploration of the fate of stirring as parcels subduct along isopycnals.

Appendix A : Effect of Discrete Lateral Sampling on Spectral Estimates

For Line P, we determine the transfer function imposed on the data by our uneven lateral sampling by making synthetic spatial series and then sampling them with the same lateral sampling used during the cruises. One thousand realizations of a red-noise process consisting of the integral of Gaussian distributed white noise is

formed on a 100 m lateral grid the same length as the section. The grid is then sampled with the exact same cast spacing as achieved during the cruise. Finally, that grid is then resampled to a 500 m grid, which is the same used to form the spectral estimates in the paper. The same spectral processing as the original time series is used.

The effect of this procedure on the spectral estimates for the Line P data shows that there is a roll-off at approximately 5 km lateral scale (Figure 20). This is consistent with a roll-off expected from the mean separation between casts of 1.7 km, which gives a $\text{sinc}^2(\Delta x) = (\sin(\pi \Delta x k_x)) / (\pi \Delta x k_x)^2$. The shapes are similar, though the effect of uneven sampling moves some variance from low wave numbers to high.

Note that these spectra are quite red, though we have whitened them for presentation, so the effects of aliasing unresolved high-wave number variance into the observed spectra should be minimal.

For IWAP, the situation is slightly more complicated because SeaSoar's saw-tooth sampling pattern means successive casts are only the nominal cast spacing at middepth, and much closer together near the top and bottom of casts. To account for this, we interpolate the cast spacing onto a 100 m horizontal grid, and then compare with a synthesized series along that grid. The response is as we might expect (Figure 21), with the top and bottom of the casts rolling off at closer to a 10 km horizontal scale, and the middepths closer to 5 km. These response functions can then be used to correct the spice spectra for lost high-wave number variance.

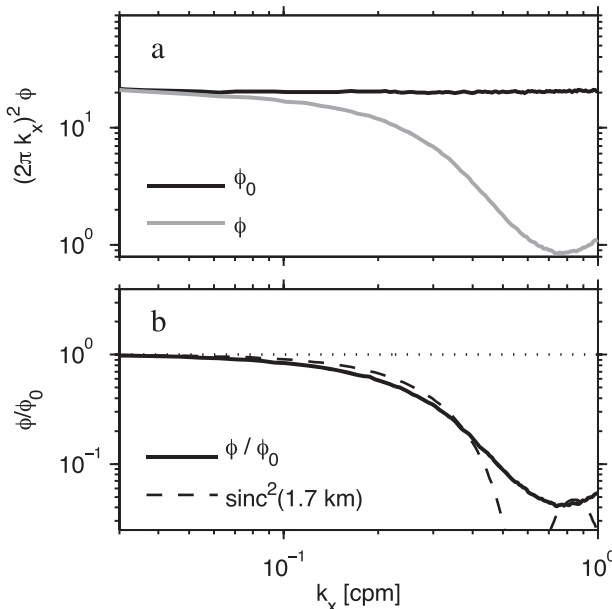


Figure 20. (a) Synthesized spectrum resolved out to high wave numbers (black) compared to the spectrum calculated by subsampling in the same manner as the shipboard sampling during Line P. (b) The empirical transfer function (solid) compared to a sinc^2 function for the mean sample distance of 1.7 km.

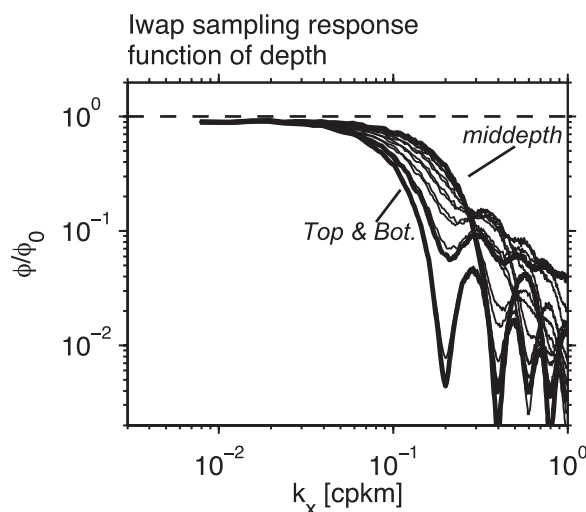


Figure 21. Synthesized spectra for a diagonal SeaSoar tow, with depths every 20 m plotted, and thick lines indicating the top, bottom, and middle of the casts. Mid-depth spectra are the best resolved, while those at the top and bottom of the drops are poorly resolved.

Acknowledgments

Thanks to Marie Robert who manages the Line P sampling program at the Institute of Ocean Sciences and the other Line P participants who helped with data collection, including Ian Beveridge. Conversations with Raffael Ferrari, Eric Kunze, Dan Rudnick, and Sylvia Cole were very helpful. The three reviewers, including Shafer Smith, greatly helped to improve this manuscript, with a large number of helpful corrections, suggestions, and clarifications. The data used in this paper are available by request to the lead author: jklymak@uvic.ca. The data collection was supported by Canadian National Science and Engineering Research Council, grant: 327920-2006 and NSF grants OCE-0425283 and OCE-0424717.

References

- Alford, M. H., J. A. MacKinnon, Z. Zhao, R. Pinkel, J. Klymak, and T. Peacock (2007), Internal waves across the Pacific, *Geophys. Res. Lett.*, **34**, L24601, doi:10.1029/2007GL031566.
- Batchelor, G. K. (1959), Small-scale variation of convected quantities like temperature in turbulent fluid, *J. Fluid Mech.*, **5**, 113–139.
- Boccaletti, G., R. Ferrari, and B. Fox-Kemper (2007), Mixed layer instabilities and restratification, *J. Phys. Oceanogr.*, **37**, 2228–2250.
- Boyd, J. P. (1992), The energy spectrum of fronts: Time evolution of shocks in Burger's equation, *J. Atmos. Sci.*, **49**, 128–139.
- Callies, J., and R. Ferrari (2013), Interpreting energy and tracer spectra of upper-ocean turbulence in the submesoscale range (1–200 km), *J. Phys. Oceanogr.*, **43**, 2456–2474, doi:10.1175/JPO-D-13-063.1.
- Capet, X., J. McWilliams, M. Molemaker, and A. Shchepetkin (2008), Mesoscale to submesoscale transition in the California Current System. Part I: Flow structure, eddy flux, and observational tests, *J. Phys. Oceanogr.*, **38**, 29–43.
- Charney, J. G. (1971), Geostrophic turbulence, *J. Atmos. Sci.*, **28**, 1087–1095.
- Chelton, D., R. Deszoeke, M. Schlax, K. El Naggar, and N. Siwertz (1998), Geographical variability of the first baroclinic Rossby radius of deformation, *J. Phys. Oceanogr.*, **28**, 433–460.
- Cole, S., and D. Rudnick (2012), The spatial distribution and annual cycle of upper ocean thermohaline structure, *J. Geophys. Res.*, **117**, C02027, doi:10.1029/2011JC007033.
- Cole, S., D. Rudnick, and J. Colosi (2010), Seasonal evolution of upper-ocean horizontal structure and the remnant mixed layer, *J. Geophys. Res.*, **115**, C04012, doi:10.1029/2009JC005654.
- Crawford, W. (2002), Physical characteristics of Haida eddies, *J. Oceanogr.*, **58**, 703–713.
- Crawford, W., J. Galbraith, and N. Bolingbroke (2007), Line P ocean temperature and salinity, 1956–2005, *Prog. Oceanogr.*, **75**, 161–178, doi: 10.1016/j.pocean.2007.08.017.
- Ferrari, R., and D. Rudnick (2000), Thermohaline variability in the upper ocean, *J. Geophys. Res.*, **105**, 16,857–16,884, doi:10.1029/2000JC000057.
- Garrett, C., and W. Munk (1972), Space-time scales of internal waves, *Geophys. Fluid Dyn.*, **2**, 225–264.
- Gregg, M. C., and W. C. Hess (1985), Dynamic response calibration of Sea-Bird temperature and conductivity probes, *J. Atmos. Oceanic Technol.*, **2**, 304–313.
- Gregg, M. C., and E. Kunze (1991), Shear and strain in Santa Monica Basin, *J. Geophys. Res.*, **96**, 16,709–16,719.
- Hoskins, B., and F. Bretherton (1972), Atmospheric frontogenesis models: Mathematical formulation and solutions, *J. Atmos. Sci.*, **29**, 11–37.
- Klein, P., B. L. Hua, G. Lapeyre, X. Capet, S. Le Gentil, and H. Sasaki (2008), Upper ocean turbulence from high-resolution 3D simulations, *J. Phys. Oceanogr.*, **38**, 1748–1763.
- LaCasce, J. (2008), Statistics from Lagrangian observations, *Prog. Oceanogr.*, **77**, 1–29.
- LaCasce, J. H. (2012), Surface quasigeostrophic solutions and baroclinic modes with exponential stratification, *J. Phys. Oceanogr.*, **42**, 569–580.
- MacKinnon, J., M. Alford, R. Pinkel, J. Klymak, and Z. Zhao (2013a), The latitudinal dependence of shear and mixing in the Pacific transiting the critical latitude for PSI, *J. Phys. Oceanogr.*, **43**, 3–16, doi:10.1175/JPO-D-11-0107.1.
- MacKinnon, J., M. H. Alford, O. Sun, R. Pinkel, Z. Zhao, and J. Klymak (2013b), Parametric subharmonic instability of the internal tide at 29 N, *J. Phys. Oceanogr.*, **43**, 17–28, doi:10.1175/JPO-D-11-0108.1.
- Munk, W. H. (1981), Internal waves and small-scale processes, in *Evolution of Physical Oceanography*, edited by B. A. Warren and C. Wunsch, pp. 264–291, MIT Press, Cambridge, Mass.
- Pelland, N. A., C. C. Eriksen, and C. M. Lee (2013), Subthermocline eddies over the washington continental slope as observed by seagliders, 2003–09, *J. Phys. Oceanogr.*, **43**, 2025–2053, doi:10.1175/JPO-D-12-086.1.
- Pinkel, R., L. Rainville, E. Slater, A. Goldin, L. Green, M. Bui, and T. Aja (2003), The hydrographic Doppler sonar system on the Roger Revelle, in *Proceedings of the IEEE/OES Seventh Working Conference on Current Measurement Technology*, pp. 237–239, IEEE, doi:10.1109/CCM.2003.1194320.
- Scott, R. (2006), Local and nonlocal advection of a passive scalar, *Phys. Fluids*, **18**, 116601.
- Smith, K., and R. Ferrari (2009), The production and dissipation of compensated thermohaline variance by mesoscale stirring, *J. Phys. Oceanogr.*, **39**, 2477–2501.
- Smith, K., G. Boccaletti, C. Henning, I. Marinov, C. Tam, I. Held, and G. Vallis (2002), Turbulent diffusion in the geostrophic inverse cascade, *J. Fluid Mech.*, **469**, 13–48.
- Thorpe, S. A. (1977), Turbulence and mixing in a Scottish loch, *Philos. Trans. R. Soc. London A*, **286**, 125–181.
- Todd, R., D. Rudnick, M. Mazloff, B. Cornuelle, and R. Davis (2012), Thermohaline structure in the California Current system: Observations and modeling of spice variance, *J. Geophys. Res.*, **117**, C02008, doi:10.1029/2011JC007589.
- Vallis, G. K. (2006), *Atmospheric and Oceanic Fluid Dynamics: Fundamentals and Large-Scale Circulation*, Cambridge Univ. Press, Cambridge, U. K.
- Veronis, G. (1972), Properties of seawater defined by temperature, salinity, and pressure, *J. Mar. Res.*, **30**, 227–255.
- Zhurbas, V., and I. S. Oh (2003), Lateral diffusivity and Lagrangian scales in the Pacific Ocean as derived from drifter data, *J. Geophys. Res.*, **108**(C5), 3141, doi:10.1029/2002JC001596.